




Fabricating Pt/CeO₂/N–C ternary ORR electrocatalysts with extremely low platinum content and excellent performance

Ning Tan¹, Yanhua Lei^{1,*} , Da Huo¹, Mengchao Ding¹, Guanhui Gao², Yuliang Zhang¹, Shuaiqin Yu¹, Ruixuan Yu³, Hailiang Du^{4,*}, and Liutong⁵

¹Institute of Marine Materials Science and Engineering, Shanghai Maritime University, Shanghai 201306, China

²Material Science and Nano Engineering Department, Rice University, Houston, TX 77005, USA

³College of Engineering and Applied Sciences, National Laboratory of Solid State Microstructures, Nanjing University, Nanjing 210023, China

⁴College of Mechanical and Electronic Engineering, Shanghai Jian Qiao University, Shanghai 201306, China

⁵College of Materials Science and Engineering, Qingdao University of Science and Technology, Zhengzhou Road 53, Qingdao 266000, China

Received: 11 August 2021

Accepted: 9 October 2021

Published online:

3 January 2022

© The Author(s), under exclusive licence to Springer Science+Business Media, LLC, part of Springer Nature 2021

ABSTRACT

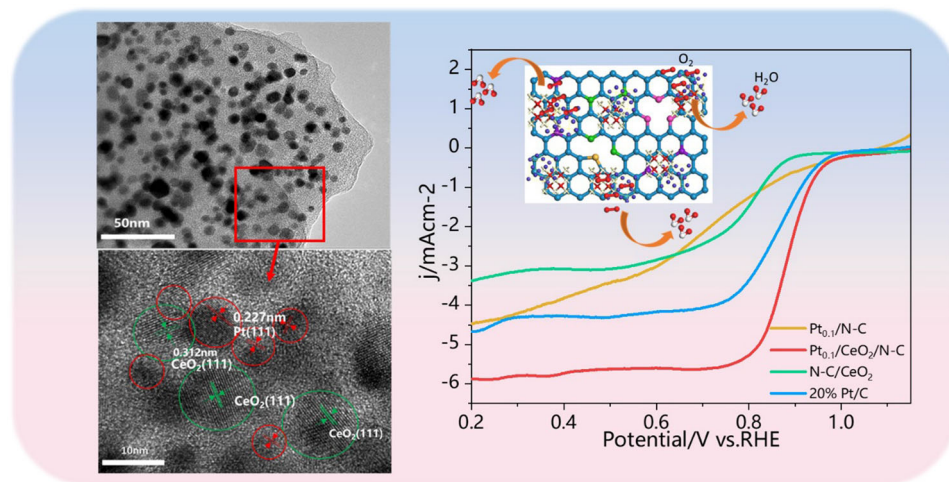
The research of high efficiency low platinum materials for oxygen reduction reaction (ORR) attracts attention in the field of energy conversion and storage. This study reports a high-efficient ternary ORR electrocatalyst containing N-doped carbon/CeO₂-supported platinum catalyst (Pt/CeO₂/N–C) with extremely low Pt content, which is fabricated by a facile two-step procedure using polyaniline (PANI) as an N source. The doped chloroplatinic anions are reduced to form evenly dispersed Pt nanoparticles (NPs) incorporated with the N-doped carbon matrix. A combination of Pt NPs with exposed highly active (111) facets, CeO₂, and active pyridinic N contributed to enhanced ORR performance and stability. The activity of our Pt_{0.1}/CeO₂/N–C catalyst containing only 5.6 wt% of Pt reaches 238.46 mA mg_{Pt}^{−1}, four times advanced than commercial 20%Pt/C catalyst (58.8 mA mg_{Pt}^{−1}). These findings reveal an important new strategy for designing high-yield and cost-effective Pt-based ORR catalysts in simple and easy way.

Handling Editor: Joshua Tong.

Ning Tan and Yanhua Lei contributed equally to the work.

Address correspondence to E-mail: yhleis@shmtu.edu.cn; hailiang_du@hotmail.com

GRAPHICAL ABSTRACT



- An important new strategy for creating low-cost and high-efficient Pt-based ternary electrocatalyst was proposed.
- Content of platinum in the resulted Pt/CeO₂/N-C catalysts is only 5 wt%, however the mass activity of the Pt_{0.1}/CeO₂/N-C material is 4.1 times higher than that of 20%Pt/C catalyst.
- The catalysts have great potential for applications as commercial catalytic materials in fuel cell.
- PtCl₆²⁻ incorporated into PANI were thermally decomposed to Pt NPs.
- Pt/N-doped C/CeO₂ exhibited an outstanding ternary synergistic ORR performance.

Introduction

Proton exchange membrane fuel cells are significant and high-effective environment-friendly energy conversion devices, capable of direct conversion of chemical energy to electric power by supporting chemical anodic (such as H₂ or alcohols oxidation) and cathodic (e.g., O₂ reduction) reactions [1, 2]. However, slow kinetics and high overpotentials throughout oxygen reduction reactions (ORRs) on the cathodes dramatically hinder their usages [3]. Currently, carbon-supported Pt-based electrocatalysts process most efficient and practical ORR ability. Nevertheless, expensiveness, poor reliability, besides

cross-effects limit their widespread industrial applications [4]. Thus, developing strongly electro-active catalysts containing less Pt with high durability need to be addressed to resolve above drawbacks [5].

The optimization of active site reactivity and their full utilization are critical factors for fabricating efficient Pt-contained ORR catalysts [6]. Thus, catalytic performances can be enhanced by regulating electronic construction and optimization of atomic arrangement on the Pt surface [7, 8]. One approach is to combine Pt particles with a catalytic support, possessing strong resistance to corrosion and sturdy interactions with Pt [9]. Carbon-based materials possess a high electrical conductivity, particularly, it can accommodate high Pt nanoparticles (NPs)

density. However, C-supported Pt catalysts would be often corroded in a harsh environment of the membrane fuel cells due to feeble interactions between Pt NPs and support carbon, which leads to catalyst particles aggregation, low catalytic ability, and declining stability [10]. The combination of metal oxides (e.g., TiO_2 , NbO_2 , SnO_2 , and CeO_2) into Pt-containing catalysts can solve this problem [11–13]. Strong interactions of these metal oxides with Pt NPs can vary their electronic structure and enhance the overall catalytic activity [14].

CeO_2 attracted high attention as a catalytic support because of its special oxygen storage and release capacity, which derived from two different valence states (Ce^{4+} , Ce^{3+}) with a unique reversible redox property, and plentiful oxygen vacancies [15]. Thus, CeO_2 is employed for encouraging the catalytic performance of Pt-contained catalysts. Enhanced oxygen electrode activities of the Pt- CeO_2 catalysts are a result of the strong electron Pt- CeO_2 interactions and the presence of the $\text{Ce}^{4+}/\text{Ce}^{3+}$ redox couple [16, 17]. Ce^{3+} cations on the CeO_2 surface act as defects and stabilize the catalytic performance, triggering the overall material more durable due to their ability of oxygen vacancies compensation. Besides, it's worth noting that CeO_2 can effectively promote the degradation of H_2O_2 , so that more effective active sites will be retained to further increase stability of the catalyst [18]. However, CeO_2 possesses poor electronic conductivity, which impedes applications of Pt- CeO_2 catalysts for ORRs. The introduction of C into the Pt- CeO_2 materials could raise the electronic conductivity without compromising sturdy interaction between Pt and CeO_2 [19, 20].

One of the most efficient ORR catalysts is N-doped C nanomaterials. N-doped C materials can significantly promote the adsorption of oxygen molecular because of N atoms acting as positively charged sites. Besides, N atoms doping results in widely distributed carbon defect sites, serving as catalytic active sites in ORR [21]. Aromatic polyaniline (PANI) is often used to produce N-doped C as it provides N and controls the desired material morphology when heated at a certain temperature. PANI also acts as a protective film to inhibit C corrosion [22, 23]. When N is introduced into the C lattice, the number of the positively charged sites increases, which is beneficial for oxygen molecules absorption and faster ORR [24–26]. Usage of CeO_2 combined with an N-doped C as composite support for Pt-based catalysts offers an

excellent potential for improving its stability and activity.

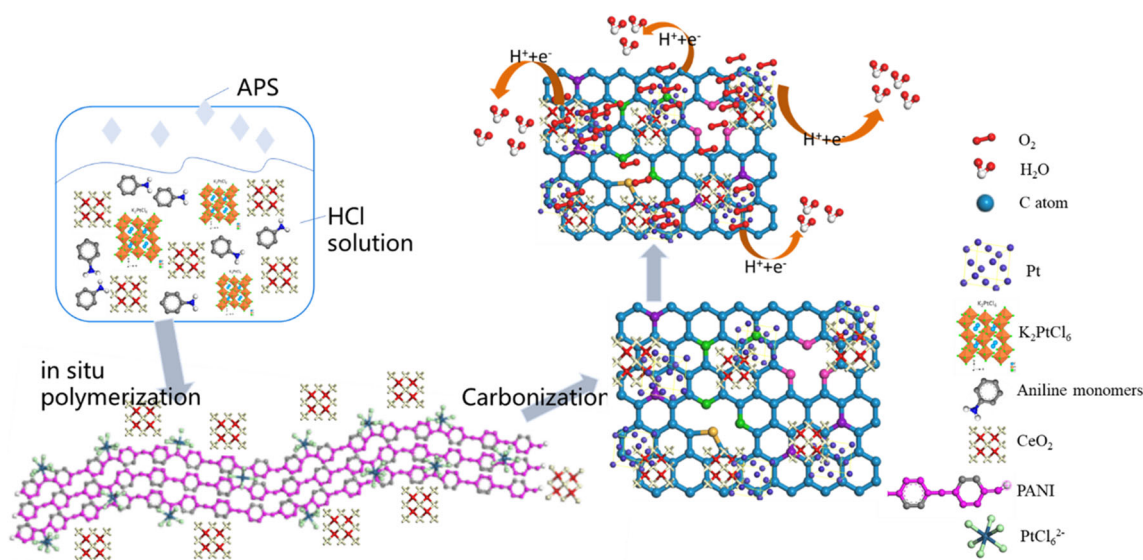
Up to now, Pt-based ternary electrocatalysts supported by carbon modified metal oxide have been reported to be a near-ideal approach to advance the ORR activity [20, 27]. Synthesis of the hybrid catalyst by combination of as-prepared individuals sequentially [28, 29], and introduction Pt into the as-prepared composite supports including carbon-encapsulated metal oxide [29, 30] were often adopted to fabricate Pt-based ternary electrocatalysts. The above strategies may face problems of intricate-steps and inefficacy in former, and reduce Pt direct contact with metal oxide, leading to poor interaction and stability in latter. Further, employment of special equipment, such as electron-deposition technology and area-selective atomic layer deposition, to achieve these specific Pt-based ternary catalysts, increase the cost of preparation and difficulty of process [31, 32]. Thus, there is thereby an urgent need but it is still a significant challenge to develop an economical strategy, with the advantages of convenience in operation and high efficiency, to develop highly active Pt-based ternary electrocatalysts with strong interaction and uniform distribution of three components.

Thus, we prepared a ternary $\text{Pt}_x/\text{CeO}_2/\text{N-C}$ composite catalyst by a facile two-step strategy with economic benefits and ease of synthesis to enhance the catalytic property and stability. $\text{Pt}_x/\text{CeO}_2/\text{PANI}$ composites with K_2PtCl_6 as doped anions for neutralizing the PANI system was synthesized, followed by a further pyrolysis treatment. The catalysts including nitrogen doping of carbon and Pt NPs anchored CeO_2 are achieved during a typical pyrolysis treatment. The well-designed catalyst exhibits surprising catalytic performance and highly long-term durability during ORR assessment.

Results

Fabrication and characterization

Scheme 1 shows the stepwise synthesis procedures. The first step is to involve aniline polymerization on the CeO_2 surface to form PANI-covered CeO_2 . Then PtCl_6^{2-} , functionalizing for charge compensation of the oxidized PANI backbone, is incorporated into the PANI matrix. The second step is PANI decomposition during the high-temperature annealing, and



Scheme 1 Preparation steps of the $\text{Pt}_x/\text{CeO}_2/\text{N-C}$ catalysts synthesis.

N-doped C forms during this stage, meanwhile Pt NPs also are fabricated (as a result of PtCl_6^{2-} decomposition) during the pyrolysis step and loading on N-C/ CeO_2 , forming a ternary $\text{Pt}_x/\text{CeO}_2/\text{N-C}$ catalyst.

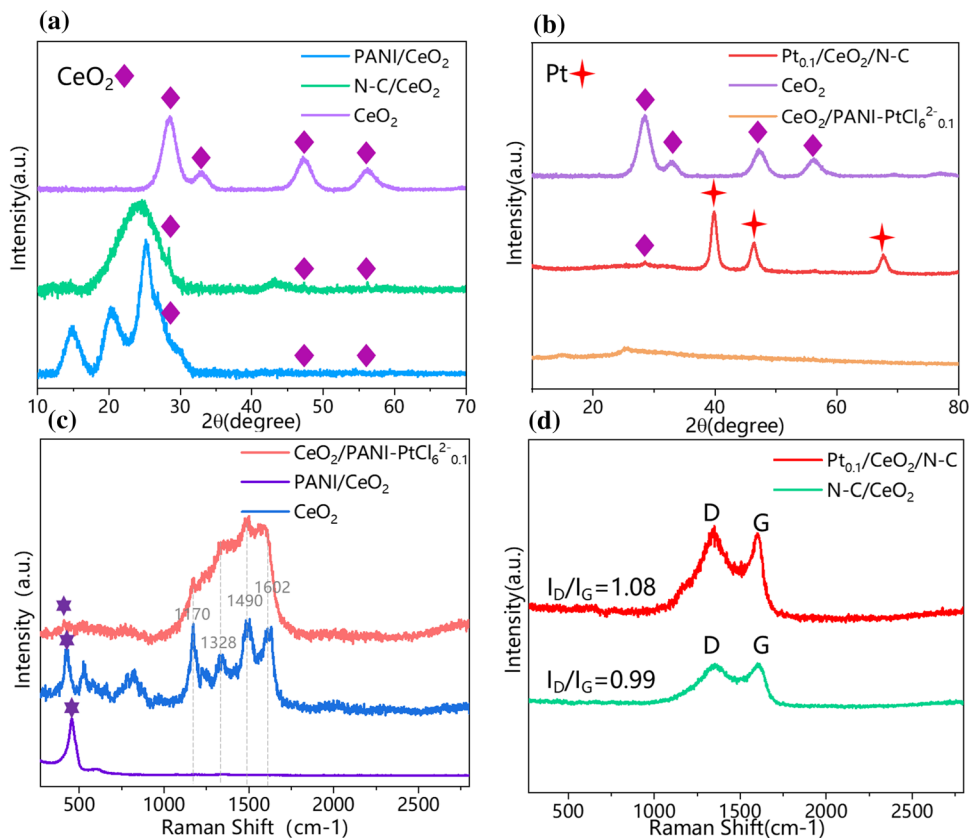
Formation of high purified fluorite-structures CeO_2 (JCPDS-43-1002) was first confirmed by XRD diffraction patterns in Fig. 1, without the presence of other Ce-containing phases diffraction. Average particle size of as-prepared CeO_2 is approximately 6.0 nm in light of Scherrer equation. XRD of N-C/ CeO_2 demonstrates a sharp peak at 26.2° , which is consonant with graphitic carbon (002) reflection and the other diffraction peaks at 28.8° , 47.8° , and 56.7° are allocated severally to $\text{CeO}_2(111)$, (220) and (311) planes, illustrating the formation of N-doped graphitic carbon/ CeO_2 composite material. A comparison of the XRD patterns of $\text{CeO}_2/\text{PANI-PtCl}_6^{2-}$ and $\text{Pt}_{0.1}/\text{CeO}_2/\text{N-C}$ indicates that a broad diffraction peak at 25.5° attributes to the PANI matrix [33] (see Fig. 1a, b). Additionally, there is no new peak appeared in the material after K_2PtCl_6 is introduced into the reaction mixture, confirming that PtCl_6^{2-} remains stable and does not decompose to Pt NPs. Several new peaks appear in the XRD pattern of $\text{Pt}_{0.1}/\text{CeO}_2/\text{N-C}$ at 39.8° , 46.3° , 67.5° , and 81.3° (see Fig. 1b), which correspond to (111), (200), (220), and (311) planes of Pt according to the PDF card number 01-087-0646. Among the planes of (111) and (311) XRD peaks of CeO_2 are detected at 28.5° and 47.3° . Thus, Pt NPs and CeO_2 coexist in this composite

material. The intensity of the Pt XRD peaks in the $\text{Pt}_x/\text{CeO}_2/\text{N-C}$ spectra ($x = 0.05\text{--}0.2$) in Fig. S1 increases as x increasing. The average diameter of the Pt NPs enlarges from 5.7 to 27.4 nm as the amount of added K_2PtCl_6 increases from 0.05 to 0.2 g, respectively. ICP-OES exhibits that the actual Pt contents in the $\text{Pt}_{0.2}/\text{CeO}_2/\text{N-C}$, $\text{Pt}_{0.1}/\text{CeO}_2/\text{N-C}$, and $\text{Pt}_{0.05}/\text{CeO}_2/\text{N-C}$ catalysts are 6.8%, 5.6%, and 5.1%, respectively. These amounts are far below commercial Pt/C catalysts containing 20 wt% of Pt.

Raman spectra $\text{CeO}_2/\text{PANI-PtCl}_6^{2-}$ and PANI/CeO_2 demonstrate vibrational bands at 410 cm^{-1} and 434 cm^{-1} of CeO_2 , and compared to the band position of the pure ceria at 458 cm^{-1} slightly peaks shift was observed [34, 35] because of the packaging of PANI on the surface of CeO_2 NPs [36]. PANI coating on CeO_2 NPs result in the appearance of bands at 1150 cm^{-1} and 1310 cm^{-1} due to stretching vibrations of C=N and C-N, and the bands at 1490 cm^{-1} and 1602 cm^{-1} associated to bending vibrations of C=C in PANI [37], as shown in Fig. 1c. These Raman results confirm the presence of PANI on the CeO_2 NP surfaces.

Samples subjected to the pyrolysis, N-C/ CeO_2 , and $\text{Pt}_{0.1}/\text{CeO}_2/\text{N-C}$, exhibited two Raman peaks at 1369 and 1598 cm^{-1} and 1350 and 1602 cm^{-1} , respectively, (see Fig. 1d), which are the D and G bands of carbon. These separately corresponds to disordered graphitic and sp^2 -hybridized C [38]. The intensity relation between the D and G bands (I_D/I_G) of $\text{Pt}_{0.1}/\text{CeO}_2/\text{N-C}$ specimen (which was equal to

Figure 1 XRD patterns of CeO_2 (top purple curve in both a, b), a CeO_2/PANI composite (material before the pyrolysis, bottom blue curve) and $\text{N-C}/\text{CeO}_2$ (catalyst formed after the pyrolysis, middle green curve) and of b $\text{CeO}_2/\text{PANI-PtCl}_6^{2-}$ (materials the before pyrolysis, middle, red curve) and $\text{Pt}_{0.1}/\text{CeO}_2/\text{N-C}$ (yellow bottom curve, catalyst formed after the pyrolysis). Raman figures of c the CeO_2 , CeO_2/PANI , and $\text{CeO}_2/\text{PANI-PtCl}_6^{2-}$ before the pyrolysis and d $\text{N-C}/\text{CeO}_2$ and $\text{Pt}_{0.1}/\text{CeO}_2/\text{N-C}$ materials obtained after the pyrolysis.



1.08) is higher than for the $\text{N-C}/\text{CeO}_2$ catalyst (which is equal to 0.99). Thus, the $\text{Pt}_{0.1}/\text{CeO}_2/\text{N-C}$ sample possesses more defective sites in the C-support.

As shown in XPS spectra of $\text{Pt}_{0.1}/\text{CeO}_2/\text{N-C}$ and $\text{CeO}_2/\text{PANI-PtCl}_6^{2-}$, peaks belonged to C and N, conforming PANI presence in the samples (see Fig. 2a). Pt, Cl, O, and S originates from the chloroplatinate and sulfate anions, respectively. A weak Ce XPS signal at ~ 940 eV is detected in the samples prepared before and after the pyrolysis. The samples subjected to the pyrolysis show weak or no Cl peaks. The disappearance of the Cl peak in the $\text{Pt}_{0.1}/\text{CeO}_2/\text{N-C}$ spectrum confirmed PtCl_6^{2-} decomposition during the pyrolysis step. As shown in Fig. 2b, Pt 4f spectrum of the $\text{CeO}_2/\text{PANI-PtCl}_6^{2-}$ sample, respectively, demonstrates two peaks at 75.9 eV and 72.7 eV, interpreting as Pt 4f_{5/2} and Pt 4f_{7/2}, which remain typical for compounds containing Pt⁴⁺ [30]. The Pt 4f peaks in the pyrolyzed catalysts shifted to ~ 74.5 eV and 71.2 eV, respectively. The last peak binding energy is almost identical to the binding energy of pure Pt (which is equal to 71.15 eV), which confirms the formation of Pt NPs. The residual two

peaks at 72.4 eV and 75.8 eV are accredited to Pt oxides (see Fig. 2d) [39].

Ce 3d XPS spectra for the $\text{Pt}_{0.1}/\text{CeO}_2/\text{N-C}$ and $\text{CeO}_2/\text{N-C}$ samples are illustrated in Fig. 2c and Fig. S3b. Owing to the CeO_2 lattice defects, Ce in CeO_2 is often presented as a mixture of Ce^{3+} and Ce^{4+} [40, 41]. The peaks resolved at 885.15 eV and 903.88 eV are signed to Ce^{3+} , while other peaks belong to Ce^{4+} . $\text{Pt}_{0.1}/\text{CeO}_2/\text{N-C}$ sample shows slightly higher Ce^{3+} content (equal to 22.59%) than $\text{N-C}/\text{CeO}_2$ sample (which contained 21.3% of Ce^{3+} , see Fig. S3b), very likely because of the partial Ce^{4+} reduction under the Pt NP presence. This observation might imply that Ce^{3+} in CeO_2 can act as a reducing agent facilitating Pt NP nucleation on the CeO_2 surface [42].

In Fig. 3e, four different categories of N were deconvoluted in the N1s XPS spectrum of the $\text{Pt}_{0.1}/\text{CeO}_2/\text{N-C}$ sample (see Fig. 2e). Peaks at 401.2 eV and 403.3 eV 398.3 eV are graphitic and oxidized N, peaks at 398.3 eV and 399.8 eV are ascribed to pyridinic and pyrrolic nitrogen [3, 43]. Percentages of these species in the total N content are shown in Fig. 3d. Graphitic and pyridinic nitrogen are typically

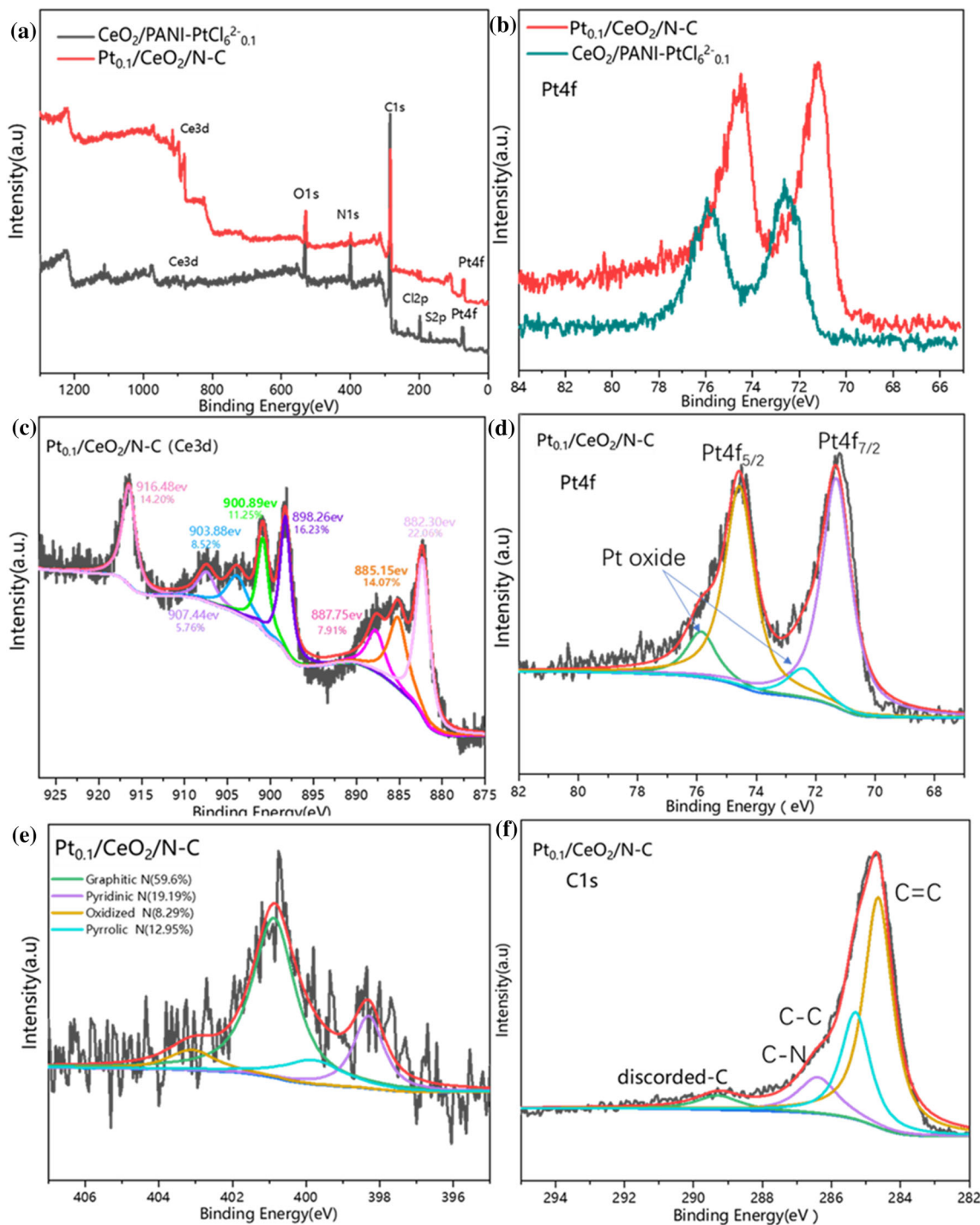
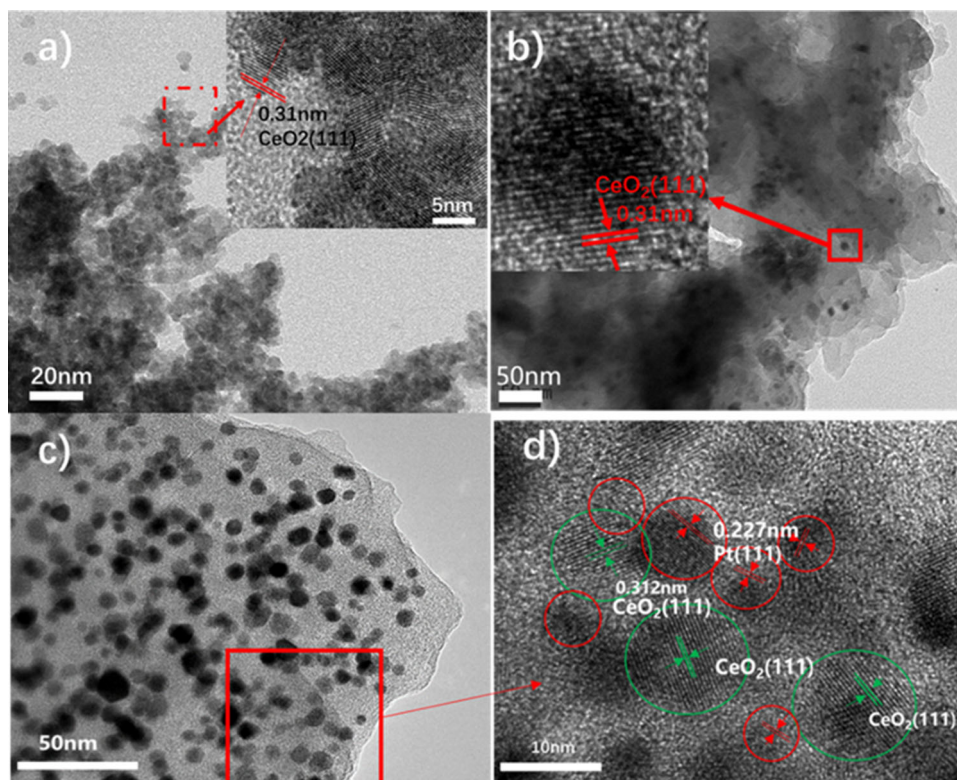


Figure 2 a XPS wide spectra and b Pt 4f of the Pt_{0.1}/CeO₂/N-C and CeO₂/PANI-PtCl₆²⁻ samples. c Ce 3d and d Pt 4f spectra of the Pt_{0.1}/CeO₂/N-C. e N 1s and f C 1s core-level spectra of the Pt_{0.1}/CeO₂/PANI.

active during ORR. Pyridine N has an unshared pair of electrons, and the electrons that are involved in the conjugated p-bond [44]. Graphitic N is energetic during electron transfer from C to O orbitals. Effect of Pt presence on the percentages of these N species is

not apparent (see Table S1). As shown in Fig. 3f, four peaks sited at 284.6, 285.2, 286.2 and 289.12 eV were resolved in the C1s spectrum of the Pt_{0.1}/CeO₂/N-C sample, consistent with the graphitic, aromatic or

Figure 3 a CeO_2 , b $\text{CeO}_2/\text{PANI-PtCl}_6^{2-}$ and c, d $\text{Pt}_{0.1}/\text{N-C}/\text{CeO}_2$ TEM and HRTEM micrographs.



aliphatic C=C bonds, C–C bonds at 285.2 eV, C–N bonds and 4) C=O bonds, correspondingly.

TEM images of the $\text{Pt}_{0.1}/\text{CeO}_2/\text{N-C}$ catalyst demonstrate agglomerated sphere-like CeO_2 NPs, 5–10 nm in size (see Fig. 3a), which agrees with the XRD results. HRTEM showed lattice fringes 0.31 nm apart, which matches to the (111) plane of CeO_2 [45]. Figure 3b shows CeO_2 NPs homogeneously disperse in the PANI matrix. EDS of the $\text{CeO}_2/\text{PANI-PtCl}_6^{2-}$ catalyst shows homogeneous distribution of C, N, Pt, and Cl (see Fig. S3), which confirms PtCl_6^{2-} presence in the PANI matrix.

Numerous small dark dots with average diameter 5 nm appear in the C substrate after pyrolysis step (see Fig. 3c and Fig. S4, Fig. S5). Lattice fringes by HRTEM analysis of these dots in Fig. 3d display of 0.227 nm and 0.312 nm apart, agreeing with Pt (111) plane and $\text{CeO}_2(111)$ planes, respectively [10, 39]. Pt and CeO_2 NPs overlapped, as shown in Fig. 3d and Fig. S4h). EDS elemental mappings confirm the uniform distribution of Pt NPs in the N–C matrix (see Fig. S4e). Partial Pt NPs distribution on the surface of CeO_2 indicates that the Pt NPs nucleate at CeO_2 surfaces during the pyrolysis and PtCl_6^{2-} decomposition. The abundance of oxygen vacancies in CeO_2 provides the nucleation sites facilitating the formation

of Pt NPs [46, 47]. Thus, Pt NPs nucleate on the defective CeO_2 surface, and large Pt– CeO_2 interface is achieved. Such Pt NPs arrangement and tight interfaces could be very beneficial for the electronic interactions and transferring, which, in turn, is excellent for improving the conductivity, catalytic activity, and enduring ORR performance of catalyst. The TEM and HR-TEM images illustrate that the average diameter of Pt NPs obvious increases in the catalysts without the presence of CeO_2 (Fig. S6).

Electrocatalytic ORR performance of the $\text{Pt}_{0.1}/\text{CeO}_2/\text{N-C}$ material

The ORR activity of the $\text{Pt}_{0.1}/\text{CeO}_2/\text{N-C}$ is analyzed using CV and associated to performance of commercial 20% Pt/C (see Fig. 4). A very strong ORR activity is observed for our catalyst judging by two strong cathodic peaks and a significantly larger area under the CV curve relative to the commercial 20%Pt/C material. Additionally, $\text{Pt}_{0.1}/\text{CeO}_2/\text{N-C}$ catalyst behavior is typical for hydrogen adsorption and desorption reactions in the 0–0.3 V range (see Fig. 4a). However, it does not reveal the peaks by the CV of $\text{Pt}_{0.1}/\text{N-C}$, further emphasizing the critical role of CeO_2 in the global act of catalyst. Moreover, Pt

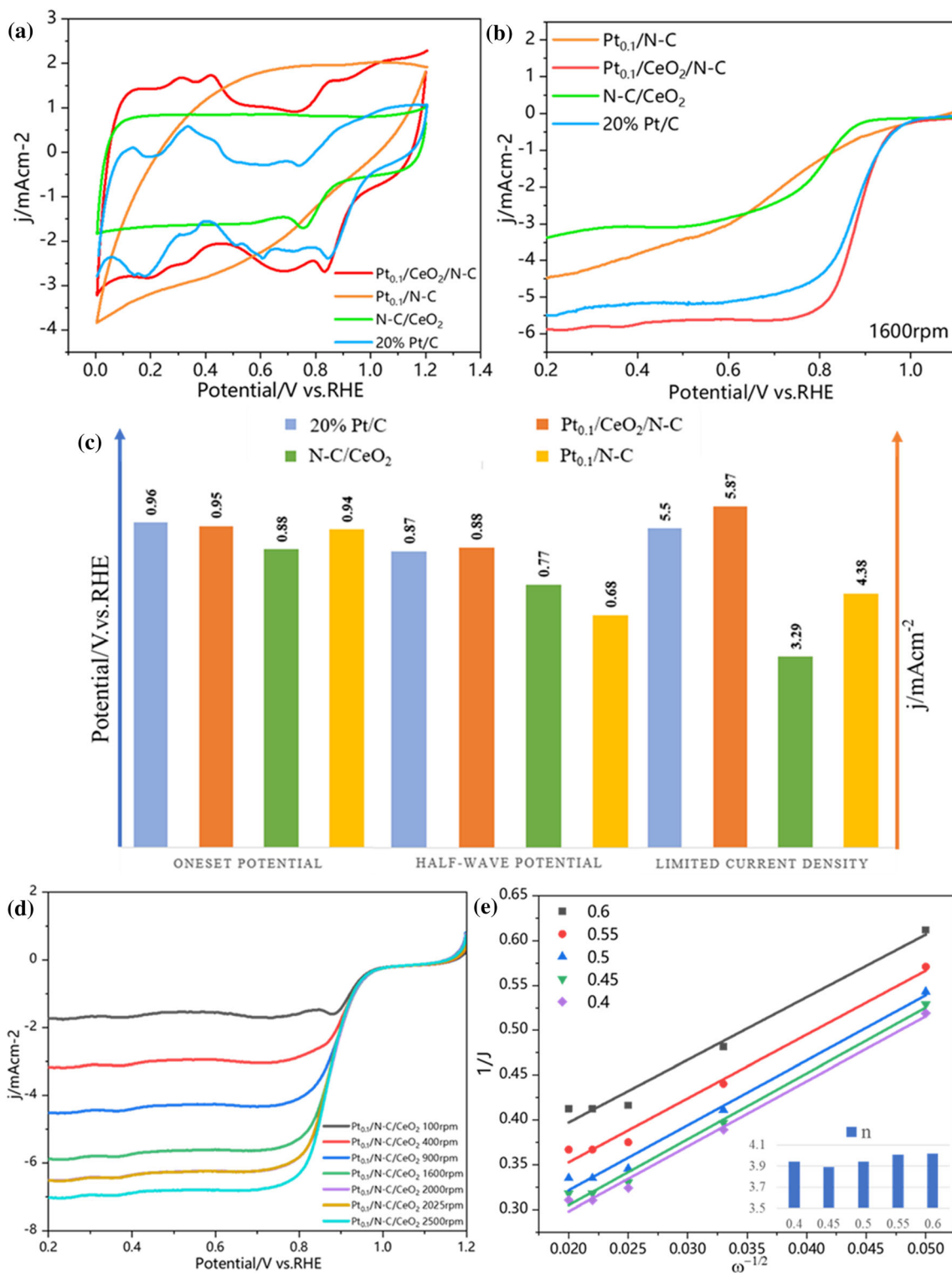


Figure 4 **a** CV and **b** LSV curves for the Pt_{0.1}/CeO₂/N-C, N-C/CeO₂, and Pt_{0.1}/N-C, 20%Pt/C catalysts recorded at 10 and 50 mV s⁻¹ sweep rates. **c** Onset, half-wave potentials and limited

current density of the Pt_{0.1}/CeO₂/N-C, N-C/CeO₂, Pt_{0.1}/N-C, and Pt/C. **d** LSV curves and **e** Koutecky-Levich (K-L) plots, besides n for the Pt_{0.1}/CeO₂/N-C catalyst.

surface oxidation is more evident for the Pt_{0.1}/N–C sample. Thus, the CeO₂ role aims to inhibit Pt oxide formation. Previous studies showed that even minor Ce³⁺ contents could suppress Pt oxide formation, especially at high voltages, by absorbing excessive oxygen from the system and converting to Ce⁴⁺ [42]. Relative to the N–C/CeO₂ sample performance during the CV tests, the ORR onset potential of the Pt_{0.1}/CeO₂/N–C catalyst significantly shifts positively, and the oxygen reduction current peak significantly enhances because of the Pt NP presence. The ternary Pt_{0.1}/CeO₂/N–C catalyst demonstrates dramatically higher overall ORR activity. Furthermore, compared to 20wt%Pt/C, the prepared ternary catalyst displays an expanded CV curve with dramatically higher current densities.

ORR performance of Pt_{0.1}/CeO₂/N–C is evaluated by LSV at 1600 rpm (presented in Fig. 4b), which shows a half-wave potential ($E_{1/2}$) at 0.19 V, and 90 mV more positive than $E_{1/2}$ of the Pt_{0.1}/N–C and N–C/CeO₂, separately (see Fig. 4c and Table S1). The limiting diffusion current density (j_l) for the Pt_{0.1}/CeO₂/N–C (which is equal to 5.88 mA cm⁻²) is advanced than Pt_{0.1}/N–C and N–C/CeO₂ catalytic agent (which are equal to 4.47 and 3.38 mA cm⁻², respectively). And the mass activity of Pt_{0.1}/CeO₂/N–C material at 0.9 V was 238.46 mA mg_{Pt}⁻¹, which was 4.1 times that of 20% Pt/C catalyst (which is 58.8 mA mg_{Pt}⁻¹). Such an excellent behavior attributes to simultaneous attendance of Pt, Ce³⁺, N in the catalyst, and catalytic synergy provided by the Pt and CeO₂ NPs and N-doped C support.

ORR kinetic parameters for the Pt_{0.1}/CeO₂/N–C obtained by LSV are recorded at varied rotating speeds. The j_l in Fig. 6d increases as the LSV rotating speed rising. The corresponding K-L results in Fig. 6e derived from LSV information express the number of the transferred electrons at 0.4–0.6 V is 3.89–4.02 (see Fig. 4e), which indicates a 4e⁻ reduction path for the Pt_{0.1}/CeO₂/N–C electrocatalyst during its participation in the ORR.

The durability of the Pt_{0.1}/CeO₂/N–C electrocatalyst and 20%Pt/C is assessed by comparing CV and LSV data before and after 2000 cycles in alkaline environment (see Fig. S7). The $E_{1/2}$ values decrease slightly after 2000 cycles during the prolonged ADP tests. Insignificant accumulation and increasing dimensions of Pt NPs during ADP tests would result in the stability degradation [30, 48–50]. However, this degradation of the Pt_{0.1}/CeO₂/N–C catalyst is still

very acceptable, which could attribute to its novel ternary structural design. The Pt NPs formed in-situ during the carbonization process, are wrapped in the carbon support. The N-doped C support improved Pt NP homogeneous dispersion and adhesion because of facilitated charge transfer from Pt to N. Additionally, forceful mutual effect between CeO₂ and Pt NPs enables formation of a stable complex, which can restrain both movement and accumulation of Pt NPs in the N-doped carbon support [51].

Discussion

Formation mechanism of the ternary heterostructure Pt_{0.1}/CeO₂/N–C catalyst

During the aniline polymerization to PANI, the [PtCl₆]²⁻ as-doped anions are distributed homogeneously in the PANI matrix to ensure consequent uniform Pt NP nucleation upon further carbonization. As the PANI matrix is pyrolyzed into an N-doped C support, [PtCl₆]²⁻ decomposed into Pt NPs. As stated by the TG-MS results in Fig. 5, the thermal decomposition of the PANI/CeO₂/[PtCl₆]²⁻ could be divided into three stages. The weight loss below 100 °C is attributed to the physically absorbed water removal judging by the fact that MS detected H₂O, CO₂, and O₂ release at 80 °C (see Fig. 5a). At 200–400 °C, 15 wt% of the catalyst weight loss occurred. The low molecular weight oligomer and doped APS and [PtCl₆]²⁻ anions undergo thermal decomposition, leading to the HCl, Cl₂, and SO₂ escaping from the system according to MS. Pt NP nucleation very likely starts at this temperature range as well. Above 400 °C, the PANI backbone is prone to decompose continuously [45]. C₂H₂ and CHN fragment release could occur above 500 °C.

Subsequently, we analyzed intermediate PANI/CeO₂/[PtCl₆]²⁻ pyrolysis products obtained at 300 °C, 400 °C, and 600 °C by XRD and TEM (see Fig. S8 and Fig. S9, respectively). XRD result from the catalyst heated to 300 °C shows a hump at 39.8°, belonging to Pt (111) plane. Based on this data, it concludes that Pt NPs nucleation occur at ~ 300 °C. Meanwhile, the decomposition of the PANI matrix result in the absence of the diffraction peaks at 20.1° (110) and 25.5°(100) [33]. The abundant Ce³⁺ in CeO₂ proving the nucleation sites facilities the formation of Pt NPs. Pt NPs are trapped at the site of the vacancies

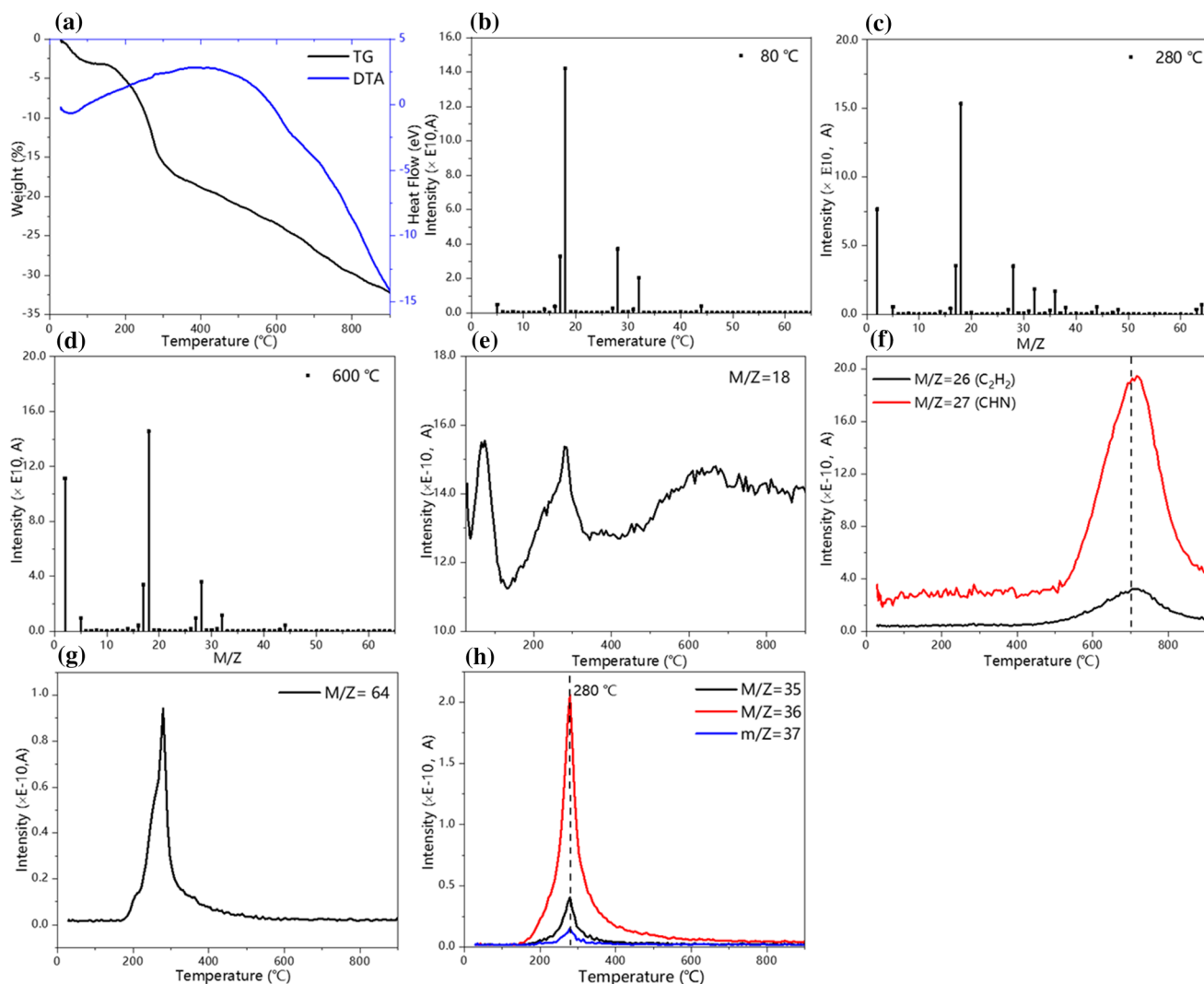


Figure 5 a TG–DTA curves of CeO₂/PANI-PtCl₆²⁻. MS results showing the evolution of gaseous species at 80 (b), 280 (c), and 600 °C (d). e–h MS results showing gaseous species evolution

from the samples prepared using different amounts of K₂PtCl₆ as a function of the temperature.

of oxygen in CeO₂ [42, 47]. From XPS evaluations in Fig. 2 and Fig. S2, Ce³⁺ presence with an increment from 21.3 to 22.59% provides the catalyst with abundant oxygen vacancies for Pt NPs to nucleate and grow. When the temperature rises to 300 °C, thermochemical reduction in the doped [PtCl₆]²⁻ occurs, converting the trapped Pt ions into the reduced metal state. As the pyrolyzed temperature increasing, more Pt NPs nucleate, the movement and coalescence of Pt NPs trigger growth of Pt NPs in diameter. Thus, the diffraction intensity of (111) Pt peak located at 39.8° increases significantly because of intensified Pt NP nucleation and growth, which is verified by XRD and TEM (see Fig. S8 and Fig. S9).

Electrocatalytic ORR performance of the Pt_{0.1}/CeO₂/N–C catalysts

According to results of electrocatalytic measurements in Fig. 4, the ternary hetero-structured Pt/CeO₂/N–C catalysts display superior ORR action in alkaline solution. Particular, we would like to emphasize that the Pt content in these materials is significantly inferior than in the commercial Pt-based catalytic agent. Content of platinum of resulted Pt/CeO₂/N–C catalysts is only 5 wt%; however, the mass activity of the Pt_{0.1}/CeO₂/N–C material at 0.9 V is 238.46 mA mgPt⁻¹, which is 4.1 times that of 20%Pt/C material (58.8 mA mgPt⁻¹). Additionally, our catalysts demonstrate an outstanding electrocatalytic stability.

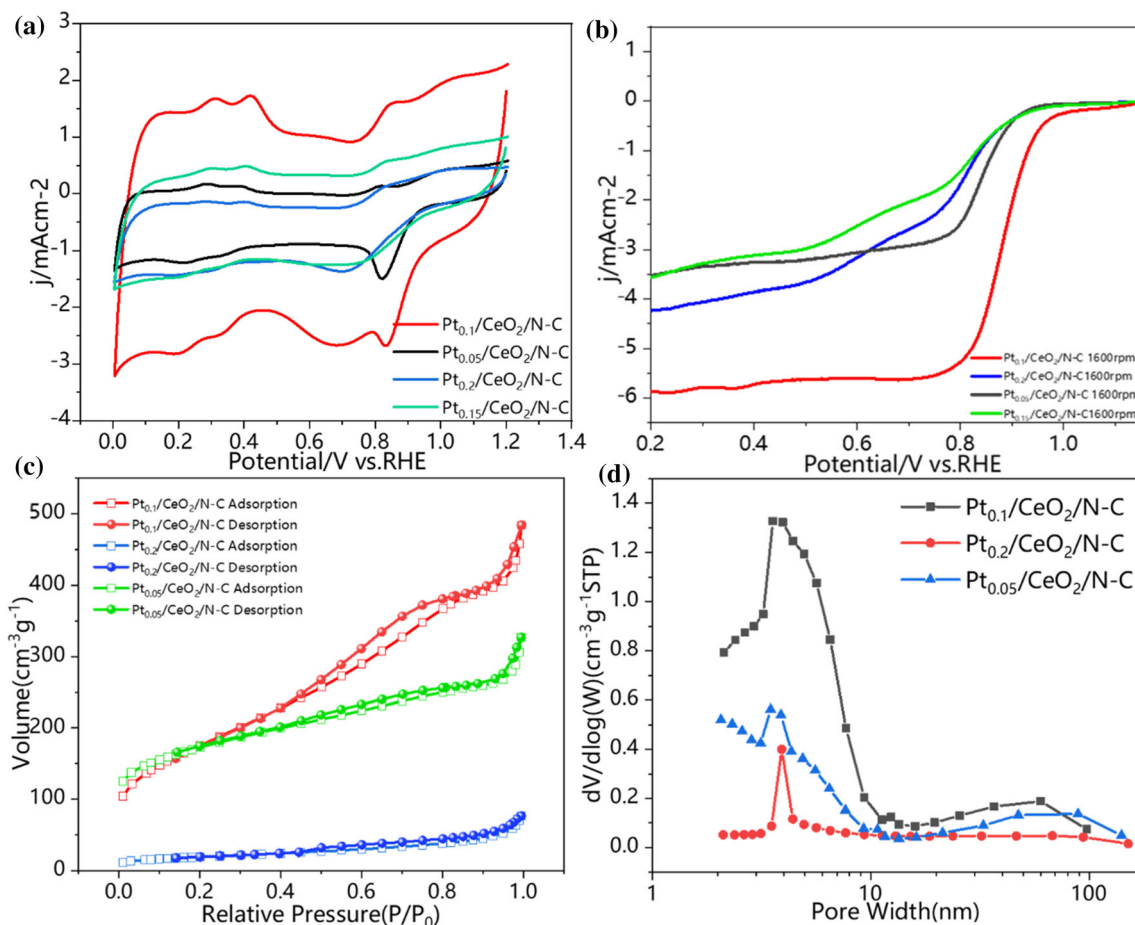


Figure 6 Pt_{0.05}/CeO₂/N-C, Pt_{0.1}/CeO₂/N-C Pt_{0.15}/CeO₂/N-C, and Pt_{0.2}/CeO₂/N-C **a** CV and **b** LSV results recorded in O₂-saturated 0.1 M KOH solution. **c** N₂ adsorption-desorption

isotherms and **d** pore size distribution results for Pt_{0.1}/CeO₂/N-C, Pt_{0.05}/CeO₂/N-C and Pt_{0.2}/CeO₂/N-C.

Table S1 compared ORR ability of lately reported Pt/CeO₂/C ternary catalyst with our catalysts. It can be seen that the ternary catalytic material reported in this paper shows the highest limited currents and mass activity.

Schematic diagram of the ternary catalyst is proposed in Scheme 1 to illustrate the excellent electrocatalyst performance. A ternary synergetic effect of individual components leads to the enhancing ORR movement. Firstly, attendance of Pt NPs dramatically shifts the onset and half-wave potential in positive direction by comparison with CeO₂/N-C. Both the results of XRD and TEM indicate Pt NPs with plentifully exposed (111) facet, in situ anchored on the CeO₂ surface and nitrogen doped carbon support, strongly increase the overall active catalyst active sites [48–52]. In return, the presence of CeO₂ in the ternary catalyst, not only play an important role in facilitating Pt NPs nucleation, but also the numerous

oxygen vacancies on the CeO₂ surface and large Pt-CeO₂ interface result in sturdy Pt-CeO₂ interactions, which can improve its ORR activity and durability. Furthermore, the Pyridinic and graphitic nitrogen atoms with their sp² electronic structures are very active ORR sites [3, 26, 55]. They enhance the material electronic conductivity and increase C corrosion resistance, which, again, can effectually advance the movement and constancy of the catalysts.

Effect of the added K₂PtCl₆ amount on the performance of the Pt_{0.1}/CeO₂/N-C catalysts

CV and LSV data of the ternary heterostructure Pt/CeO₂/N-C catalysts prepared with various K₂PtCl₆ amounts are shown in Fig. 6a, b. All CV curves displays the typical hydrogen adsorption and desorption behavior in the 0–0.3 V range. However, their

catalytic performance is strongly dependent on the amount of the K_2PtCl_6 used during the catalyst preparation. The addition of 0.1 g of K_2PtCl_6 leads to the best ORR catalytic act. The weaker presentation of the other catalysts prepared with higher K_2PtCl_6 amounts could be enlightened by formation of more Pt NPs, which is highly confirmed by both XRD and TEM measurements. The presence of excessively large Pt NPs could slow down the electrochemical activity of the ternary catalysts, since too large Pt NPs do not provide sufficient surface area. Additionally, an excessive number of Pt NPs can block the micropores of the N-doped carbon support, thus impeding oxygen diffusion. Figure 6c, d demonstrates the nitrogen adsorption/ desorption isotherms and pore size distribution of the as-prepared samples equipped with diverse K_2PtCl_6 amounts.

The specific surface area was significantly affected through amount of Pt loaded. $Pt_{0.2}/CeO_2/N-C$ has an isotherm which exhibits the II-type curve, and its BET surface area remains $68.3 \text{ m}^2 \text{ g}^{-1}$, as shown in Table S2, both of which indicate a nonporous structure. The surface areas of $Pt_{0.1}/CeO_2/N-C$ and $Pt_{0.05}/CeO_2/N-C$ samples were significantly higher, 637.0 and $603.7 \text{ m}^2 \text{ g}^{-1}$, respectively. Hierarchical porous structure is noticed with average pore diameter of 4.13 nm in $Pt_{0.1}/CeO_2/N-C$. The hierarchical porous structure grows in specific surface area which provides plentiful energetic spots for catalytic reaction, meanwhile porosity facilitates the transfer of reactants, promotes the occurrence of catalytic response, and thus improves catalytic ability.

Conclusion

This study demonstrates an innovative approach for fabricating low platinum content $Pt_{0.1}/CeO_2/N-C$ ternary catalyst with Pt highly uniformly dispersion. Accompanied by the thermal decomposition of polyaniline/ CeO_2 into N-doped carbon/ CeO_2 support, numerous Pt NPs nucleate and grow in-situ from the doped $PtCl_6^{2-}$ anions in polymeric precursor during carbonization, resulting in the porous heterostructure $Pt_{0.1}/CeO_2/N-C$ with extraordinary surface area. An optimal amount of K_2PtCl_6 addition was obtained during synthesis of PANI/ CeO_2 catalyst precursor for further fabricating the $Pt_{0.1}/CeO_2/N-C$ ternary catalyst with the largest specific surface area (equal to $637.0 \text{ m}^2 \text{ g}^{-1}$) and porosity (0.66

$\text{cm}^3 \text{g}^{-1}$). The resulting ternary catalysts exhibit excellent electrochemical properties in 0.1 M KOH solutions. Comparison with 20% Pt/C materials (with activity equal to 58.8 mA mg Pt), the activity of our $Pt_{0.1}/CeO_2/N-C$ catalyst (containing only 5.6 wt% of Pt) is four times higher, equal to 238.46 mA mg Pt . The $Pt_{0.1}/CeO_2/N-C$ catalyst processes positive half-wave potential at 0.88 V, limit current density valued at 5.88 mA/cm^2 (vs. 0.87 V and 5.50 mA/cm^2 of 20% Pt/C, respectively) and enhanced electrochemical permanency. The improved ORR act is ascribed to the unique $Pt_{0.1}/CeO_2/N-C$ ternary interconnected structure, in which collaboration of Pt and CeO_2 modifies electronic environment of Pt surface, and N-doped carbon scaffold improves catalyst stability and conductivity. These findings reveal an important new strategy for creating affordable and high-efficient Pt-founded ternary electrocatalyst, which should thus have great potential for applications as commercial catalytic materials in fuel cell.

Supporting information

Experimental details for all as-prepared catalysts, including initial materials and chemicals, synthesis approaches, as well as characterization and electrochemical measurements methods details and other supporting information

Acknowledgements

This work was supported by National Natural Science Foundation of China (NSFC Grant No. 51602195, 11804152), the Natural Science Foundation of Shanghai (Grant No. 19ZR1422200), the Shandong Provincial Natural Science Foundation (No. ZR2019QEM004), and Foundation of Shanghai Engineering Technology Research Centre of Deep Offshore Material (19DZ2253100).

Supplementary Information: The online version contains supplementary material available at <http://doi.org/10.1007/s10853-021-06610-w>.

References

- [1] Lemes G, Sebastian D, Pastor E, Lazard MJ (2019) N-doped graphene catalysts with high nitrogen concentration for the oxygen reduction reaction. *J Power Sources* 438:10
- [2] Mistry H, Varela AS, Kühl S, Strasser P, Cuenya BR (2016) Nanostructured electrocatalysts with tunable activity and selectivity. *Nat Rev Mater* 1:16009
- [3] Han H, Noh Y, Kim Y, Jung WS, Park S, Kim WB (2019) An N-doped porous carbon network with a multidirectional structure as a highly efficient metal-free catalyst for the oxygen reduction reaction. *Nanoscale* 11:2423–2433
- [4] Markovi NM, Schmidt TJ, Stamenkovi V, Ross PN (2001) Oxygen reduction reaction on Pt and Pt bimetallic surfaces: a selective review. *Fuel Cells* 1:105–116
- [5] Gasteiger HA, Kocha SS, Sompalli B, Wagner FT (2005) Activity benchmarks and requirements for Pt, Pt-alloy, and non-Pt oxygen reduction catalysts for PEMFCs. *Appl Catal B Environ* 56:9–35.
- [6] Stamenkovic VR, Fowler B, Mun BS, Wang G, Ross PN, Lucas CA, Markovic NM (2007) Improved oxygen reduction activity on Pt₃Ni(111) via increased surface site availability. *Science* 315:493–497
- [7] Kitchin JR, Nørskov JK, Barteau MA, Chen JG (2004) Modification of the surface electronic and chemical properties of Pt(111) by subsurface 3d transition metals. *J Chem Phys* 120:10240–10246
- [8] Strasser P, Koh S, Anniyev T, Greeley J, Nilsson A (2010) Lattice-strain control of the activity in dealloyed core-shell fuel cell catalysts. *Nat Chem* 2:454–460
- [9] Cheng Y, Lu H, Zhang K, Yang F, Dai W, Liu C, Dong H, Zhang X (2018) Fabricating Pt-decorated three dimensional N-doped carbon porous microspherical cavity catalyst for advanced oxygen reduction reaction. *Carbon* 128:38–45
- [10] Du C, Gao X, Cheng C, Zhuang Z, Li X, Chen W (2018) Metal organic framework for the fabrication of mutually interacted Pt CeO₂ ternary nanostructure: advanced electrocatalyst for oxygen reduction reaction. *Electrochim Acta* 266:348–356
- [11] Huang K, Li Y, Yan L, Xing Y (2014) Nanoscale conductive niobium oxides made through low temperature phase transformation for electrocatalyst support. *RSC Adv* 4:9701
- [12] Tan Q, Du C, Sun Y, Yin G, Gao Y (2014) Pd-around-CeO₂-X hybrid nanostructure catalyst: three-phase-transfer synthesis, electrocatalytic properties and dual promoting mechanism. *J Mater Chem A* 5:1429–1435
- [13] Ignaszak A, Teo C, Ye S, Gyenge ED (2010) Pt-SnO₂/Pd/C electrocatalyst with enhanced activity and durability for the oxygen reduction reaction at low Pt loading: the effect of carbon support type and activation. *J Phys Chem C* 114:16488–16504
- [14] Kakinuma K, Chino Y, Senoo Y, Uchida M, Kamino T, Uchida H, Deki S, Watanabe M (2013) Characterization of Pt catalysts on Nb-doped and Sb-doped SnO₂ support materials with aggregated structure by rotating disk electrode and fuel cell measurements. *Electrochim Acta* 110:316–324
- [15] Chirambatte Peter SC, Ramani S, Sarkar S, Vemuri V (2017) Chemically designed CeO₂ nanoboxes boost the catalytic activity of Pt nanoparticles toward electro-oxidation of formic acid. *J Mater Chem A* 5:11572–11576
- [16] Xu H, Wang A-L, Tong Y, Li G-R (2016) Enhanced catalytic activity and stability of Pt/CeO₂/Pani hybrid hollow nanorod arrays for methanol electrooxidation. *ACS Catal* 6:5198–5206
- [17] Kaur B, Srivastava R, Satpati B (2016) Highly efficient CeO₂ decorated nano-ZSM-5 catalyst for electrochemical oxidation of methanol. *ACS Catal* 6:2654–2663
- [18] Bai S, Zhang X, Yu Y, Li J, Yang Y, Wei H, Chu H (2019) Fabricating nitrogen-rich Fe–N/C electrocatalysts through CeO₂ assisted pyrolysis for enhanced oxygen reduction reaction. *ChemElectro Chem* 6:4040–4048
- [19] Lim DH, Lee WD, Choi DH, Lee HI (2010) Effect of ceria nanoparticles into the Pt/C catalyst as cathode material on the electrocatalytic activity and durability for low-temperature fuel cell. *Appl Catal B Environ* 94:85–96
- [20] Luo Y, Calvillo L, Daiguebonne C, Daletou MK, Granozzi G, Alonso-Vante N (2016) A highly efficient and stable oxygen reduction reaction on Pt/CeO_x/C electrocatalyst obtained via a sacrificial precursor based on a metal-organic framework. *Appl Catal B Environ* 189:39–50
- [21] Xia W, Mahmood A, Liang Z, Zou R, Guo S (2016) Earth-abundant nanomaterials for oxygen reduction. *Angew Chem Int Ed* 55:2650–2676
- [22] Luo Y, Estudillo-Wong LA, Cavillo L, Granozzi G, Alonso-Vante N (2016) An easy and cheap chemical route using a MOF precursor to prepare Pd–Cu electrocatalyst for efficient energy conversion cathodes. *J Catal* 338:135–142
- [23] Ye B, Cheng K, Li W, Liu J, Mu S (2017) Polyaniline and perfluorosulfonic acid Co-stabilized metal catalysts for oxygen reduction reaction. *Langmuir* 33:5353–5356
- [24] Lu YC, Gasteiger HA, Yang SH (2011) Catalytic activity trends of oxygen reduction reaction for nonaqueous Li-air batteries. *J Am Chem Soc* 133:19048–19051
- [25] Bashyam R, Zelenay P (2006) A class of non-precious metal composite catalysts for fuel cells. *Nature* 443:63–66
- [26] Jiang Z, Yu J, Huang T, Sun M (2018) Recent advance on polyaniline or polypyrrole-derived electrocatalysts for oxygen reduction reaction. *Polymers* 10:1397

- [27] Mori T, Ou DR, Zou J, Drennan J (2012) Present status and future prospect of design of Pt-cerium oxide electrodes for fuel cell applications. *Prog Nat Sci* 22:561–571
- [28] Wang X, Li XY, Liu DP, Song SY, Zhang HJ (2012) Green synthesis of Pt/CeO₂/graphene hybrid nanomaterials with remarkably enhanced electrocatalytic properties. *Chem Commun* 48:2885–2887
- [29] Wei YC, Zhao Z, Liu J, Xu CM, Jiang GY, Duan AJ (2013) Design and synthesis of 3D ordered macroporous CeO₂-supported Pt@CeO₂-delta core-shell nanoparticle materials for enhanced catalytic activity of soot oxidation. *Small* 9:3957–3963
- [30] Sun W, Sun J, Du L, Du C, Gao Y, Yin G (2016) Synthesis of nitrogen-doped niobium dioxide and its Co-catalytic effect towards the electrocatalysis of oxygen reduction on platinum. *Electrochim Acta* 195:166–174
- [31] Xu H, Wang AL, Tong YX, Li GR (2016) Enhanced catalytic activity and stability of Pt/CeO₂/PANI hybrid hollow nanorod arrays for methanol electro-oxidation. *ACS Catal* 6:5198–5206
- [32] Cheng NC, Banis MN, Liu J, Riese A, Li X, Li RY, Ye SY, Knights S, Sun XL (2015) Extremely stable platinum nanoparticles encapsulated in a zirconia nanocage by area-selective atomic layer deposition for the oxygen reduction reaction. *Adv Mater* 27:277–281
- [33] Sadak O, Prathap MA, Gunasekaran S (2019) Facile fabrication of highly ordered polyaniline–exfoliated graphite composite for enhanced charge storage. *Carbon* 144:756–763
- [34] MingYan W, Wei Z, DongEn Z, ShuAn L, WeiXing M, ZhiWei T, Jun C (2014) CeO₂ hollow nanospheres decorated reduced graphene oxide composite for efficient photocatalytic dye-degradation. *Mater Lett* 137:229–232
- [35] Sun L, Zhou L, Yang C, Yuan Y (2017) CeO₂ nanoparticle-decorated reduced graphene oxide as an efficient bifunctional electrocatalyst for oxygen reduction and evolution reactions. *Int J Hydrogen Energy* 42:15140–15148
- [36] Kumar S, Ojha AK, Patrice D, Yadav BS, Materny A (2016) One-step in situ synthesis of CeO₂ nanoparticles grown on reduced graphene oxide as an excellent fluorescent and photocatalyst material under sunlight irradiation. *PCCP* 18:11157–11167
- [37] Zhu J, Xu Y, Wang J, Wang J, Bai Y, Du X (2015) Morphology controllable nano-sheet polypyrrole–graphene composites for high-rate supercapacitor. *PCCP* 17:19885–19894
- [38] Jiang S, Sun Y, Dai H, Hu J, Ni P, Wang Y, Li Z, Li Z (2015) Nitrogen and fluorine dual-doped mesoporous graphene: a high-performance metal-free ORR electrocatalyst with a super-low HO₂⁻ yield. *Nanoscale* 7:10584–10589
- [39] Zhang C, Zhang R, Li X, Chen W (2017) PtNi nanocrystals supported on hollow carbon spheres: enhancing the electrocatalytic performance through high temperature annealing and electrochemical Co stripping treatments. *ACS Appl Mater Interfaces* 9:29623–29632
- [40] Shi Q, Ma Y, Qin L, Tang B, Yang W, Liu Q (2019) Metal-free hybrid of nitrogen-doped nanocarbon@carbon networks for highly efficient oxygen reduction electrocatalyst. *ChemElectroChem* 6:2924–2930
- [41] Concepción P, Corma A, Silvestre-Albero J, Franco V, Chane-Ching JY (2004) Chemoselective hydrogenation catalysts: Pt on mesostructured CeO₂ nanoparticles embedded within ultrathin layers of SiO₂ binder. *J Am Chem Soc* 126:5523–5532
- [42] Du JS, Bian T, Yu J, Jiang Y, Wang X, Yan Y, Jiang Y, Jin C, Zhang H, Yang D (2017) Embedding ultrafine and high-content Pt nanoparticles at ceria surface for enhanced thermal stability. *Adv Sci* 4:1700056
- [43] Lin Z, Waller GH, Liu Y, Liu M, Wong C-P (2013) 3D nitrogen-doped graphene prepared by pyrolysis of graphene oxide with polypyrrole for electrocatalysis of oxygen reduction reaction. *Nano Energy* 2:241–248
- [44] Deng H, Li Q, Liu J, Wang F (2017) Active sites for oxygen reduction reaction on nitrogen-doped carbon nanotubes derived from polyaniline. *Carbon* 112:219–229
- [45] Lei Y, Qiu Z, Tan N, Du H, Li D, Liu J, Liu T, Zhang W, Chang X (2020) Polyaniline/CeO₂ nanocomposites as corrosion inhibitors for improving the corrosive performance of epoxy coating on carbon steel in 3.5% NaCl solution. *Prog Org Coat* 139:105430
- [46] Spezzati G, Su Y, Hofmann JP, Benavidez AD, DeLaRiva AT, McCabe J, Datye AK, Hensen EJM (2017) Atomically dispersed Pd-O species on CeO₂(111) as highly active sites for low-temperature Co oxidation. *ACS Catal* 7:6887–6891
- [47] Xu F, Wang D, Sa B, Yu Y, Mu S (2017) One-pot synthesis of Pt/CeO₂/C catalyst for improving the ORR activity and durability of pemfc. *Int J Hydrogen Energy* 42:13011–13019
- [48] Sun Y, Zhang X, Luo M, Chen X, Wang L, Li Y, Li M, Qin Y, Li C, Xu N, Lu G, Gao P, Guo S (2018) Ultrathin PtPd-based nanorings with abundant step atoms enhance oxygen catalysis. *Adv Mater* 30:1802136
- [49] Bu L, Ding J, Guo S, Zhang X, Su D, Zhu X, Yao J, Guo J, Lu G, Huang X (2015) A general method for multimetallic platinum alloy nanowires as highly active and stable oxygen reduction catalysts. *Adv Mater* 27:7204–7212
- [50] Gao S, Lin Y, Jiao X, Sun Y, Luo Q, Zhang W, Li D, Yang J, Xie Y (2016) partially oxidized atomic cobalt layers for carbon dioxide electroreduction to liquid fuel. *Nature* 529:68–71

- [51] Liu H, Zhong P, Liu K, Han L, Zheng H, Yin Y, Gao C (2018) Synthesis of ultrathin platinum nanoplates for enhanced oxygen reduction activity. *Chem Sci* 9:398–404
- [52] Zhao X, Dai L, Qin Q, Pei F, Hu C, Zheng N (2017) Self-supported 3D PdCu alloy nanosheets as a bifunctional catalyst for electrochemical reforming of ethanol. *Small* 13:1602970
- [53] An H, Zhang R, Li Z, Zhou L, Shao M, Wei M (2016) Highly efficient metal-free electrocatalysts toward oxygen reduction derived from carbon nanotubes@polypyrrole core-shell hybrids. *J Mater Chem A* 4:18008–18014

Publisher's Note Springer Nature remains neutral with regard to jurisdictional claims in published maps and institutional affiliations.